Confidential manuscript submitted to *EPSL*
Version of Record: https://www.sciencedirect.com/science/article/pii/S0012821X19306624
Manuscript_df70528839afba44ee5a99e3db8e8ca6

Temporal and spatial variations in seismic anisotropy and V_P/V_S ratios in a region of slow slip

Hubert Jerzy Zal[1], Katrina Jacobs[2], Martha Kane Savage[1], Jefferson Yarce[3,4], Stefan Mroczek[1,5], Kenny Graham[1], Erin K. Todd[6], Jenny Nakai[3,4], Yuriko Iwasaki[7,8], Anne Sheehan[3,4], Kimihiro Mochizuki[7], Laura Wallace[2,9], Susan Schwartz[10], Spahr Webb[11], Stuart Henrys[2]

[1]Victoria University of Wellington, Wellington, New Zealand
[2]GNS Science, Lower Hutt, New Zealand
[3]Department of Geological Sciences, University of Colorado Boulder, Boulder, Colorado, USA
[4]Cooperative Institute for Research in Environmental Sciences, University of Colorado Boulder, Boulder, Colorado, USA
[5]Now at: GFZ German Research Centre for Geosciences, Potsdam, Germany and Freie University Berlin, Germany
[6]Department of Geology, University of Otago, Dunedin, New Zealand
[7]Earthquake Research Institute, University of Tokyo, Tokyo, Japan
[8]Now at: Japan Meteorological Agency, Tokyo, Japan
[9]Institute for Geophysics, University of Texas, Austin, Texas, USA
[10]Department of Earth and Planetary Sciences, University of California, Santa Cruz, California, USA
[11]Lamont-Doherty Earth Observatory, Columbia University, Palisades, New York, USA

Keywords: Subduction zones, slow slip, seamount, New Zealand, Shear wave splitting, anisotropy

Corresponding author: Hubert Zal, `hubert.zal@vuw.ac.nz`

Abstract

In September 2014, a five week long slow slip event (SSE) occurred near Gisborne at the northern Hikurangi subduction zone, New Zealand, and was recorded by offshore instruments deployed by the Hikurangi Ocean Bottom Investigation of Tremor and Slow Slip (HOBITSS) project. Up to 25 cm of slip occurred directly below the HOBITSS array. We calculate shear wave splitting (SWS) and V_P/V_S ratios for event-station pairs on HOBITSS ocean bottom seismometers and onshore GeoNet seismic stations to determine the relationship in time and space between slow slip and these seismic properties. Spatial averaging of SWS fast azimuths yields trench-perpendicular fast azimuths in some areas, suggesting that compressive stress from plate convergence closes microcracks and controls anisotropy in the upper-plate. Variations from the trench perpendicular directions are observed near a subducting seamount, with directions closely resembling fracture and fault patterns created by subducting seamounts previously observed in both laboratory and field experiments. Temporal variations in fast azimuths are observed at three stations, two of which are located above the seamount, suggesting measurable variations in stress orientations. During the SSE, median V_P/V_S measurements across all offshore stations increase from 1.817 to 1.894 and SWS delay times decrease from 0.178 s to 0.139 s (both changes are significant within 95% confidence intervals). Temporal variations in V_P/V_S and delay time are consistent with fluid pressurization below a permeability barrier and movement of fluids during the rupture of a slow-slip patch.

1 Introduction

Slow slip events (SSEs) are characterized as slow, earthquake-like motions that release energy over periods ranging from days to years. Understanding the physical processes occurring during SSEs is particularly important from an earthquake hazard perspective, as SSEs may influence the timing of nearby large earthquakes (e.g., *Obara and Kato*, 2016), or alternatively be triggered by earthquakes (e.g., *Wallace et al.*, 2018). The driving mechanisms behind the occurrence and nucleation of SSEs are still poorly understood, but observational and modelling studies suggest that SSEs arise in the transition zone between velocity strengthening (i.e., aseismic creep) and velocity weakening (i.e., stick slip) behavior on the plate interface, possibly in the presence of high fluid pressures (e.g., *Audet et al.*, 2010).

From May 2014 to June 2015, the Hikurangi Ocean Bottom Investigation of Tremor and Slow Slip (HOBITSS) project deployed 15 Ocean Bottom Seismometers (OBS) and 24 Absolute Pressure Gauges (APG) with the goal of recording offshore seismological and geodetic data during an SSE (*Wallace et al.*, 2016). From late September to late October 2014 an SSE occurred offshore Gisborne, directly below the HOBITSS array (Figure 1; *Wallace et al.*, 2016). The September-October 2014 Gisborne SSE is the first in New Zealand to be recorded by offshore instruments.

Here, we use local earthquake data from nine HOBITSS OBSs and nine GeoNet permanent land-based seismic stations to determine crustal anisotropy, where most S-phases travel directly from the source to receiver. As a shear wave enters a seismically anisotropic medium it is split into two orthogo-

nally polarized quasi-shear waves with a fast and slow polarization (*Crampin*, 1981). The anisotropy is represented by two splitting parameters; Φ, the polarization of the fast azimuth (or "fast azimuth") of the anisotropic material and δt, the delay time accrued during the travel through the anisotropic material. The delay time is dependent on the path length within the anisotropic material and the difference between the velocity of the fast and slow polarized waves. If anisotropy changes along the path, the splitting will be most sensitive to the last layer traversed (e.g., *Rumpker and Silver*, 1998).

In the crust, anisotropy is mainly caused by either pre-existing structural features, such as faults and dikes, or by the preferential closing of microcracks at particular orientations as a response to horizontal differential stresses (*Babuska and Cara*, 1991). In the upper crust, fast azimuths tend to be parallel to fluid filled microcracks and to the maximum principal stress (*Crampin*, 1981). Differential horizontal stress will preferentially close the cracks that are oriented orthogonal to the maximum horizontal compressive stress ($S_H max$; *Nur*, 1971). Cracks tend to close completely with depth due to lithostatic pressure. Therefore, most studies of upper crustal anisotropy find little change in splitting with depth, suggesting that the top few kilometers are most important for splitting measurements (e.g., *Savage et al.*, 2010). Cracks are also important in controlling the ratio of the speeds of seismic compressional and shear waves, V_P/V_S. With higher quantities of liquid-filled cracks, S wave velocities are reduced more than P waves and hence the ratio increases (*Nur*, 1971). In this paper we use the complementary sensitivity of V_P/V_S and SWS measurements to cracks in the upper crust to evaluate the stress field before, during and after the September-October 2014 SSE.

1.1 Hikurangi Subduction Zone and the September-October 2014 SSE

The Pacific and Australian plates converge through the North Island region at ~50 mm/yr, at an oblique angle to the orientation of the plate boundary (Figure 1; e.g., *Wallace et al.*, 2004). Slip is partitioned with the trench perpendicular component accommodated on the subduction thrust, and a trench parallel component largely accommodated by upper-plate strike-slip faulting and clockwise rotation of the North Island forearc (*Beanland and Haines*, 1998; *Wallace et al.*, 2004). North Island's main geological features, such as the Raukumara mountain ranges and the North Island Dextral Fault Belt, tend to follow a trench parallel, NNE-SSW, direction (*Beanland and Haines*, 1998). Focal mechanisms from the Raukumara Peninsula region show a maximum compressive stress that is trench parallel in the overriding plate (*Townend et al.*, 2012).

Since 2002, more than 30 SSEs have been documented and observed in New Zealand using continuous Global Positioning System data (cGPS; e.g., *Wallace and Eberhart-Phillips*, 2013; *Wallace et al.*, 2016). These events vary in duration, from six days to 1.5 years, with equivalent moment release from Mw 6.3-7.2, depths from 2-60 km, and recurrence intervals of 2 to 5 years (e.g., *Wallace and Beavan*, 2010). The SSEs occurring offshore the east coast of the northern Hikurangi trench are of particular interest due to their shallow depth (less than 15 km), shorter recurrence intervals (<2 years), short du-

ration (a few weeks or less) and large horizontal deformation signals (1-3 cm) on onshore stations (e.g., *Wallace and Beavan*, 2010; *Wallace et al.*, 2016).

A total of four SSEs (SSE1-SSE4) occurred within close proximity to the HOBITSS array during the deployment; the timing of SSE1-4 were calculated from time-dependent geodetic inversions by *Warren-Smith et al.* (2019). SSE1, the earliest and longest, occurred south of the array, between September and November 2014. The September-October 2014 SSE (SSE2) started 20 days after the start of SSE1, directly beneath the array and was the largest and best recorded SSE; it was recorded on APGs as well as onshore permanent cGPS stations (Figure 1; *Wallace et al.*, 2016). We emphasize the main pulse of SSE2, between Julian days 265-285. Tremor and repeating earthquakes began a few days before day 285 (*Todd et al.*, 2018; *Shaddox and Schwartz*, 2019). SSE2 tails off between days 286-300 (*Warren-Smith et al.*, 2019), so that the extended period of SSE2 is five weeks long; the tremor and repeating earthquakes continue throughout the tail-off period. The vertical deformation resolved from the HOBITSS APGs during SSE2 enabled better delineation of the trench-ward extent of SSEs and suggests that slip occurred to within 2 km of the seafloor, and perhaps all the way to the trench (*Wallace et al.*, 2016). SSE3 occurred in December 2014 just southwest of the array and SSE4 occurred in February 2015, also southwest of the array.

1.2 Previous Results

1.2.1 Shear Wave Splitting Results

Previous SWS analyses across the Raukumara Peninsula using local earthquakes have shown mainly trench-parallel fast azimuths, ranging from ~0° to 30°, on the eastern side of the Raukumara Peninsula, and larger variations in azimuths further west (Figure 1; *Head*, 2001; *Audoine et al.*, 2004; *Unglert*, 2011). Our dataset complements that of previous studies and extends crustal splitting results offshore for the first time.

1.2.2 V_P/V_S

Typically, V_P/V_S ratios are thought to increase when fluid pressures approach lithostatic, or in areas with high clay content (e.g., *Eberhart-Phillips et al.*, 2017). Tomographic studies have shown that regions of slow-slip have elevated fluid pressures and tend to have high Poisson's ratios and high V_P/V_S ratios (e.g., *Audet et al.*, 2010). Seismic attenuation (*Eberhart-Phillips et al.*, 2017) and residual travel-times (*Bassett et al.*, 2014) are both higher in the Northern Hikurangi trench than they are further south for similar depths. This is consistent with a more fluid-rich system in the north. The source area of a deep SSE occurring in Central Hikurangi, ~100 km southwest of the September-October 2014 SSE, coincides with a high V_P/V_S area, ranging from ~1.7-1.8, and is interpreted as a fluid-rich and highly over-pressurized region (*Wallace and Eberhart-Phillips*, 2013). The subduction interface is located at ~15 km beneath the Gisborne area, with a westerly 10° dip (*Williams et al.*, 2013). Subduct-

ing seamounts are imaged between the east coast of the Raukumara Peninsula and the Hikurangi trench (Figure 1; *Bell et al.*, 2010), and many more seamounts protrude above the sedimentary cover on the not-yet subducted Pacific Plate. Zones of high-amplitude interface reflectivity are associated with these subducting seamounts and have been interpreted as entrained fluid-rich sediments that may promote slow slip (*Bell et al.*, 2010). These high-amplitude reflectivity regions of the plate interface are associated with high V_P/V_S (~1.8) and low seismic attenuation ratios (Qs/Qp <1; *Eberhart-Phillips et al.*, 2017).

Temporal and spatial variations in V_P/V_S have been observed during large earthquakes and SSEs. *Husen and Kissling* (2001) found an increase in V_P/V_S above a suggested permeability barrier following the 1995, 8.0 Mw, Antofagasta Earthquake on the plate interface in Chile. They proposed that a permeability barrier allows lithostatic pore pressures to build along the seismogenic zone while hydrostatic pore pressures remain in the overlying crust. Furthermore, they suggest that only large earthquakes, such as the Mw 8 Antofagasta earthquake, can break these permeability barriers on a scale large enough to induce enough fluid flow to change V_P/V_S observations. However, observations by *Nakajima and Uchida* (2018) in Kanto Japan show cyclic variations in seismic attenuation and seismicity rates with the occurrence of SSEs and conclude that such permeability barriers may also break during SSEs. Recently, *Warren-Smith et al.* (2019) helped support this model; they used focal mechanisms from the HOBITSS OBS dataset to show that both crustal stress and fluid pressure temporally evolve through SSE cycles, suggesting that recurring breaches of permeability barriers also occur in the Hikurangi subduction zone in regions of shallow slow slip.

2 Data

The HOBITSS OBSs consisted of 10 Lamont-Doherty Ocean Bottom Seismograph Instrument Pool (OBSIP) broadband OBS (LOBS) and five University of Tokyo/Earthquake Research Institute short period OBS (EOBS; *Wallace et al.*, 2016). The array was deployed offshore Gisborne from May 2014 to June 2015 and complemented the onshore GeoNet network (Figure 1). We have calculated the horizontal orientations of the HOBITSS OBS receivers using both a P-wave (*Zietlow*, 2016) and Rayleigh wave (*Stachnik et al.*, 2012) method (Section S1). The earthquakes used for orientation analyses are presented in Table S1 and our orientation results are presented in Table S2 and provide the basis for further analyses using all three components in the HOBITSS project. LOBS1, 2, 4, 5, 6, and 10 had instrument problems and/or did not acquire enough data for instrument orientation and are omitted from further analysis in this study. Using the HOBITSS earthquake catalog of *Yarce et al.* (2019), with our depth constraint (<50 km depth), yields 2,140 earthquakes with magnitudes ranging from ML 0-4.73 (Figure 2). The median depth of the earthquakes is 23 km, with most earthquakes occurring in the subducting plate. We manually picked an additional 14,311 P and S arrivals at offshore stations EOBS1-5 and LOBS3, 7, 8, and 9. We combined these picks with 32,394 P and S arrivals from *Yarce et al.* (2019) on the same nine offshore stations and nine onshore GeoNet stations (CNGZ, KNZ, MHGZ, MWZ,

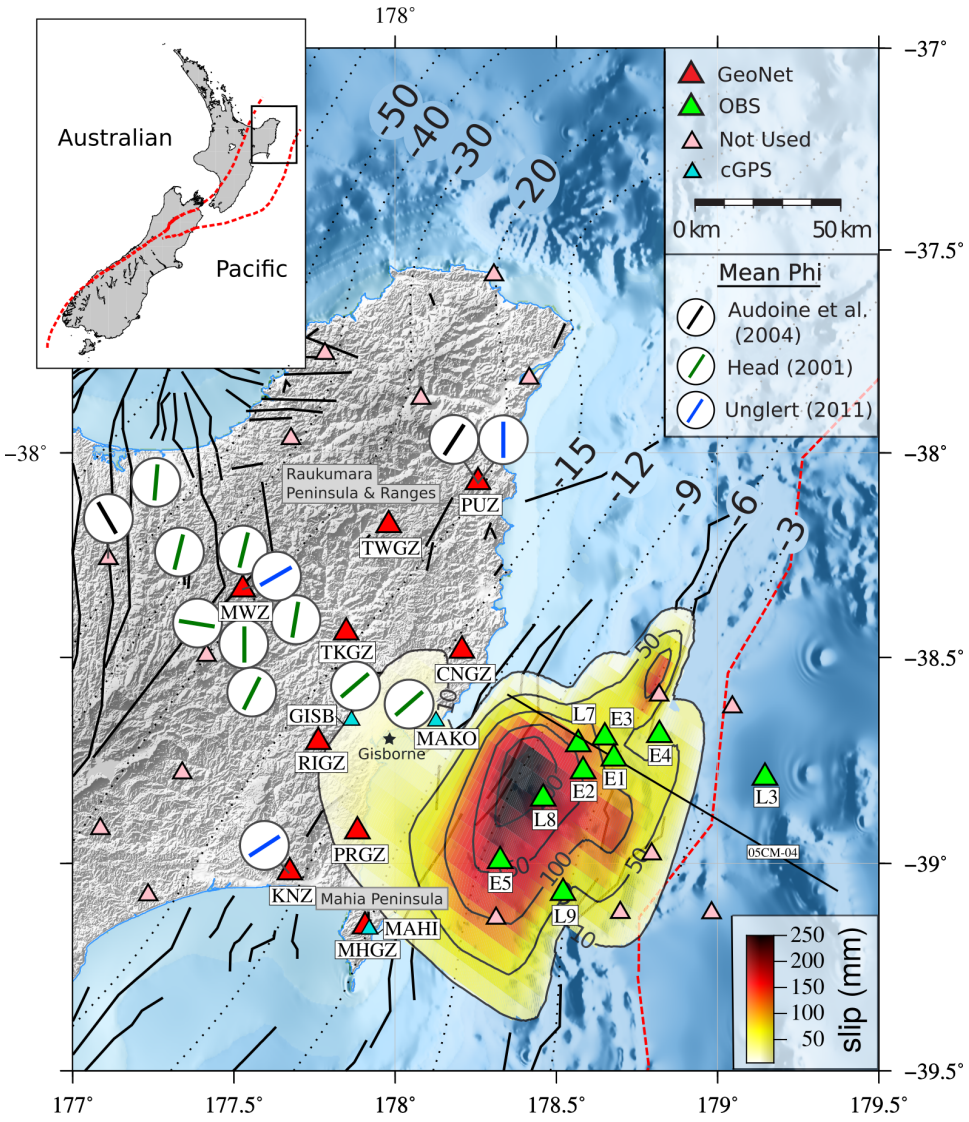

Figure 1. Locations of onshore Geonet (http://www.geonet.org.nz) seismic stations (red triangles) and HOBITSS ocean bottom seismometers (green triangles) off the coast of Gisborne (EOBS, short period ocean bottom seismometers; LOBS, broadband ocean bottom seismometers). Station names have been shortened from LOBS and EOBS to L and E. Pink triangles represent seismic stations not used in this study. Blue triangles are GeoNet cGPS stations. Mean fast azimuths from previous studies have been plotted inside white circles. Slip contours (in mm) for the September-October 2014 SSE (SSE2) are from *Wallace et al.* (2016); dotted contours of plate interface (in km) are from *Williams et al.* (2013); dashed red line of plate boundary interface is from *Coffin et al.* (1998); black line marked 05CM-04 is a 2-D seismic profile (*Barker et al.*, 2009); solid black lines of active faults are from *Litchfield et al.* (2014).

PRGZ, PUZ, RIGZ, TKGZ, TWGZ), resulting in 15,072 P-S phase pairs, where both P and S arrivals were present on the same seismogram.

Stations LOBS3, 7 and 9 experienced timing issues. These timing issues do not affect SWS results but could alter V_P/V_S results. To test for systematic affects from these stations we compared the V_P/V_S results for stations with and without timing errors (Section S2; Figure S1). We find only minor differences in these two subsets, so these stations are included in the analyses.

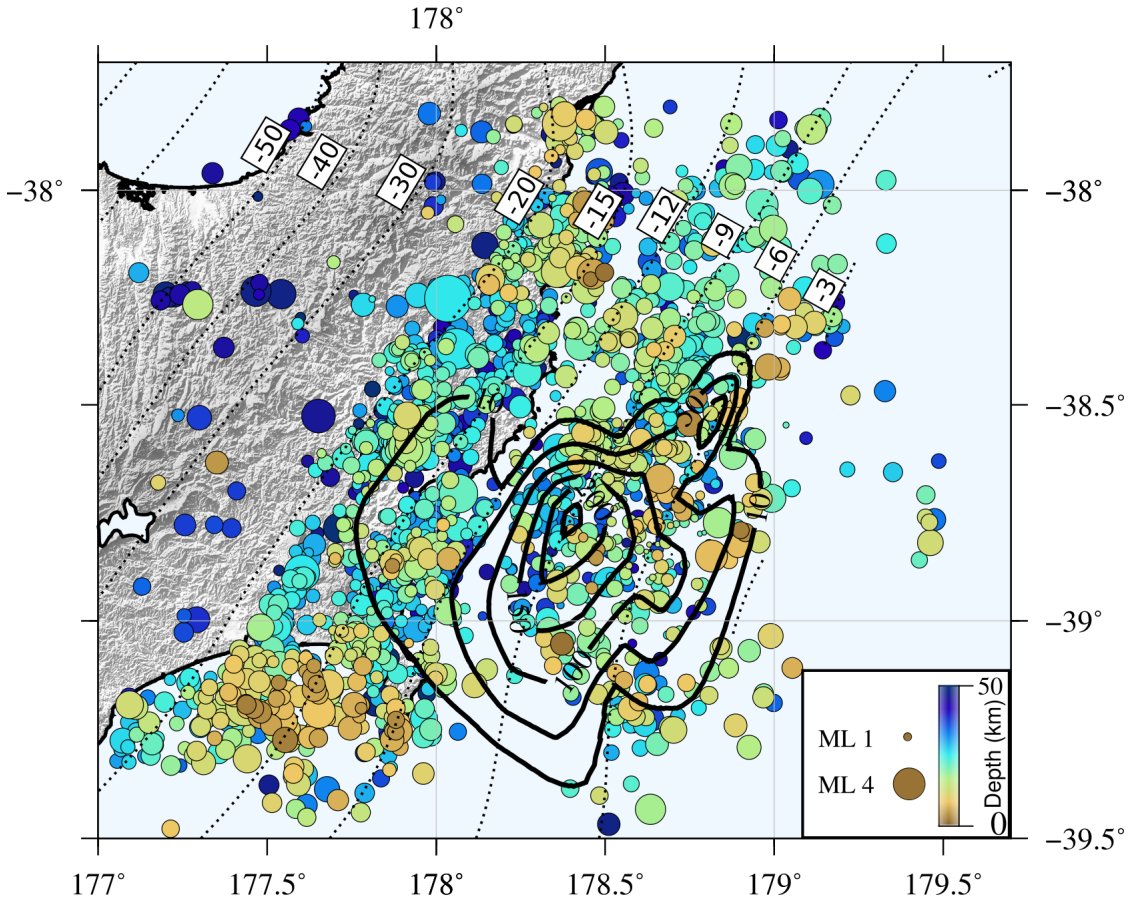

Figure 2. Earthquake locations in our study area, and above 50 km depth, selected from the HOBITSS catalog (*Yarce et al.*, 2019). The catalog runs between May 2014 to June 2015 and earthquake magnitudes (ML) range from 0 to 4.73. Slip contours for SSE2 (in mm) are from *Wallace et al.* (2016); dotted contours of plate interface (in km) are from *Williams et al.* (2013).

3 Methods

3.1 Automatic Shear Wave Splitting (MFAST)

The splitting was analysed using MFAST (Multiple Filter Automatic Splitting Technique; *Savage et al.*, 2010). MFASTv2.2 executes the following steps: (1) apply multiple band-pass filters on the S arrival waveform and calculate the best product of signal-to-noise ratio (SNR) and bandwidth; (2) apply the SWS algorithm of *Silver and Chan* (1991) to perform a grid search over the fast azimuth and delay time parameter space and determine the best parameters that correct for splitting, measured by the minimum of the smallest eigenvalue of the corrected particle motion; (3) automatically analyse multiple measurement windows, whose length is based on the period of the wave and whose starting values depend on the S arrival, using the *Silver and Chan* (1991) methods, and determine the best window using the cluster analysis technique of *Teanby et al.* (2004); (4) assign a grade from A to D, based on the SNR, uncertainty, distinctiveness of the cluster, and whether the measurement is a null (*Savage et al.*, 2010).

The incidence angle for each event-station pair was determined using the Taup Toolkit (*Crotwell et al.*, 1999) with a 1-D velocity model created for the study area from the 3-D model by *Eberhart-Phillips et al.* (2010). Because rays with incidence angles greater than 35 degrees from vertical are outside the shear wave window, they were excluded from the analyses (*Nuttli*, 1961). Delay times typically show more scatter compared to fast azimuths (e.g., *Gao and Crampin*, 2006). We used both A and B grade measurements for our analyses (examples are shown in Figures S2 and S3, respectively).

3.2 V_P/V_S

We calculated the ratio of P- to S-velocities at each station for all 15,072 P-S phase pairs (10,035 offshore, 5,037 onshore). Not limited to A and B grade measurement criteria, the quantity of phase pairs was larger than that for SWS analysis. Following the approach of *Wadati and Oki* (1933) we calculated an average ratio of P- to S-velocity (V_P/V_S) along the ray path from the arrival times at each station:

$$V_P/V_S = t_S/t_P \tag{1}$$

where $t_S = T_S - T_O$ and $t_P = T_P - T_O$, with T_S and T_P being the arrival times of the S- and P- wave, respectively, and T_O is the origin time of the earthquake.

3.3 Moving Averages and 95% Confidence Intervals

To look for temporal changes at each station, we determined the moving median values of all V_P/V_S and SWS delay time measurements. We calculated the 95% confidence intervals (CIs) of the median using the method of *Altman et al.* (2000) (Section S3). Generally, the median is more robust than the mean, and less sensitive to outliers, but is difficult to apply to azimuthal values. Therefore, temporal analysis of fast azimuths uses circular means with confidence intervals determined by bootstrapping (Section S3).

We chose a 20-day window, with a window step of 1 day, after examining several window lengths. The 20-day time window was narrow enough to reveal changes within the 35 day-long SSE2 without excessive smoothing and wide enough to provide acceptable confidence intervals. The 20-day moving windows are plotted at the center of the window, so any observed changes could start 10 days earlier or later.

3.4 Spatial Averaging

To calculate spatial averages of fast azimuths, (Φ), we used the Tomography Estimation and Shear-wave-splitting Spatial Average (TESSA) package by *Johnson et al.* (2011) over a spatial area focused on the SSE region and using a subset of 1,893 earthquakes. TESSA works by gridding the area and then assigning the fast azimuths for each earthquake to every spatial grid-block through which the ray passed. To account for potential overprinting of Φ later in the path, the individual Φ values within each grid-

block are weighted inversely proportional to the square of the distance from the station. We assigned a minimum block size of 3 km which resulted in 10-65 rays passing through each grid-block (Figure S4). Fast azimuths were not plotted for blocks with standard deviation of the average greater than 30° and standard error larger than 10° and for areas with sparse raypath coverage (mainly in the eastern study area; Figure S4).

4 Results

4.1 Fast Azimuths and Spatial Averaging

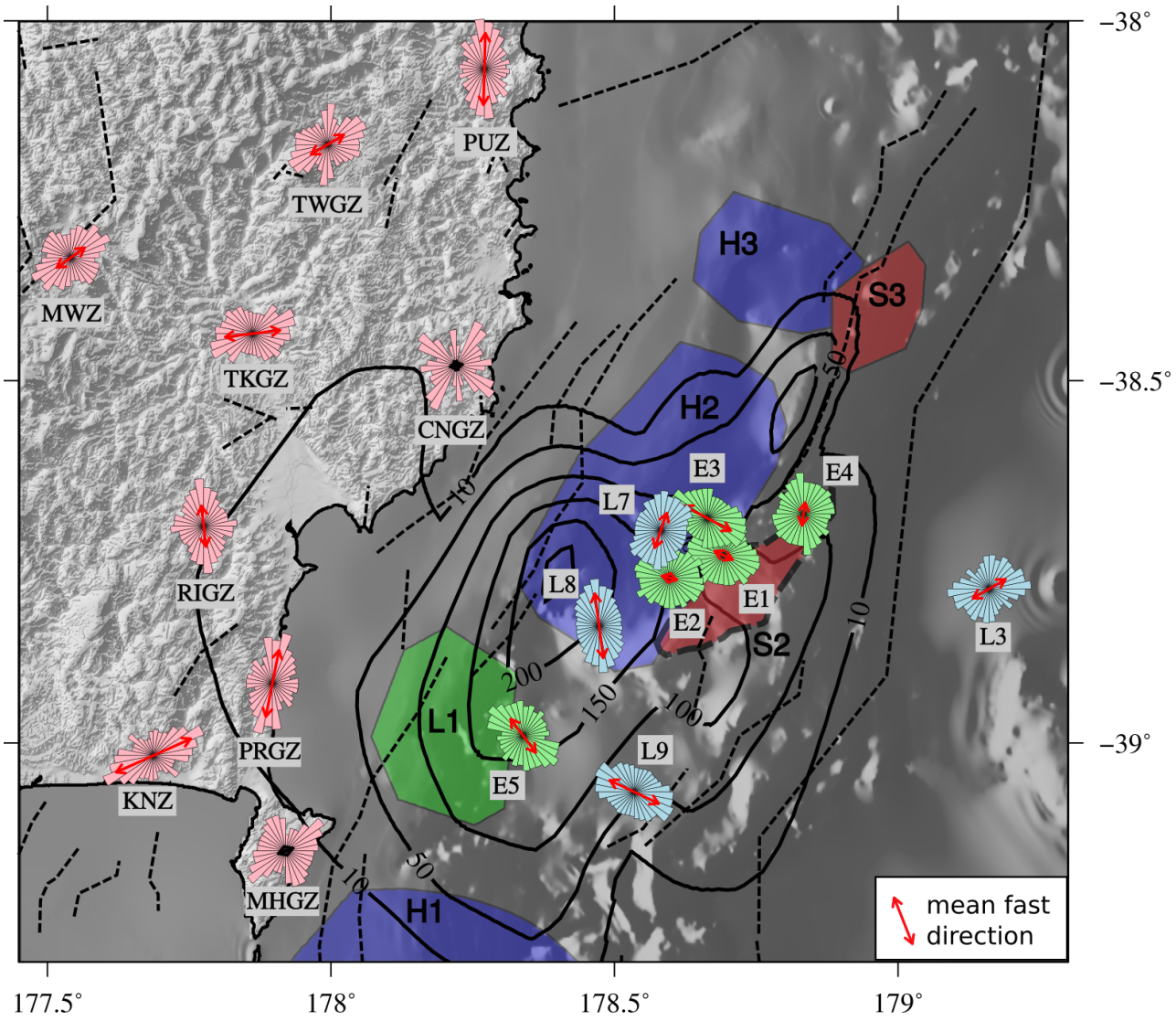

Figure 3. Rose diagrams of fast azimuths calculated using MFAST (*Savage et al.*, 2010). Rose diagrams are plotted on the stations at which measurements were made. The lengths of the sectors are proportional to the square root of the number of measurements in each sector. Red arrows are the means and are scaled by their resultant length. *S2* and *S3* indicate areas of seamounts. *H1*, *H2*, and *H3* indicate high-amplitude reflectivity zones and *L1* is a lens reflectivity zone (*Bell et al.*, 2010), with updated *S2* boundary from *Barker et al.* (2018). Slip contours (in mm) for SSE2 are from *Wallace et al.* (2016). Dashed black lines mark active faults from *Litchfield et al.* (2014).

A total of 10,676 splitting measurements (8,333 offshore and 2,343 onshore) yielded A and B grades. Figure 3 shows rose diagrams of the fast azimuths plotted at the station at which measurements were made. Mean fast azimuths vary across both onshore and offshore stations. To distinguish stations with significant mean fast azimuths from those with uniformly distributed fast azimuths, we used a Rayleigh test for circular uniformity (Rayleigh test p-value <0.05 shows a significant mean fast azimuth). All stations, except CNGZ and MHGZ, have significant mean azimuths with more than 100 measurements (Table 1). Therefore, CNGZ and MHGZ were excluded from the station average interpretation.

We observe complexity in the rose diagrams and in the spatially averaged fast azimuths (Figures 3 and 4). A trench-perpendicular NW-SE mean Φ azimuth is observed in the southern offshore region, across stations LOBS9 and EOBS5. The NW-SE trend is disrupted near the western, downdip, portion of seamount *S2* and across the related high-amplitude reflectivity zone *H2*, similar to changes observed in mean fast azimuths at stations EOBS1, 2, 3 and LOBS7 in Figure 3. Onshore stations PRGZ, RIGZ, and PUZ show a N-S trending mean azimuth. Stations MWZ and TWGZ have a NE-SW azimuth, station KNZ has a ENE-WSW azimuth and TKGZ has an azimuth closer to E-W.

4.2 Temporal changes in Fast Azimuths, Delay Time and V_P/V_S Measurements

Figure 5 shows V_P/V_S, δt, and Φ for individual offshore stations as a function of time. Stations LOBS9 and EOBS1 and 4 experience large changes in Φ but their calculated 95% confidence intervals are large and span ~180° at certain times. Station LOBS9 exhibits a ~180° change in Φ before SSE2, with Φ rotating from ~-70° (NW-SE) to ~90° (E-W) between Julian days 240 and 270. LOBS9 is located south of seamount *S2*, on a bend in the slip contours. Stations EOBS1 and EOBS4 exhibit a ~90° rotation in Φ during SSE2, between Julian days 255-310. EOBS1 rotates from ~135° (NW-SE) to ~30° (NE-SW). EOBS4 rotates from ~0° (N) to ~-70° (NW-SE). Both stations EOBS1 and EOBS4 are located between seamount *S2* and associated high-amplitude reflectivity zone *H2*. Φ at stations LOBS3, 7, 8 and EOBS2, 3 and 5 are generally more stable with time.

An increase in V_P/V_S occurs at all offshore stations during the main slip pulse of SSE2 (Figure 5). A decrease in delay times occurs during SSE2 at stations EOBS2, 3, 4, and 5, and LOBS3. Station EOBS1 and LOBS7, 8 and 9 exhibit relatively stable delay times during this period. Thus, at five stations, we observe both a decrease in delay time and increase in V_P/V_S during SSE2.

Because the majority of raypaths travel through or directly above the SSE patch, we stack the temporal V_P/V_S and SWS delay time measurements to help reinforce variations seen at individual stations (Figure 6). The stacking highlights a regional decrease in V_P/V_S starting at Julian day 248, from 1.860; CIs [1.844, 1.872] to 1.817; CIs [1.806, 1.830], over the 15 days leading up to SSE2. During SSE2 V_P/V_S increases from 1.817 to 1.894; CIs [1.882,1.907]. Following the main slip pulse (Julian day 285), V_P/V_S decreases back to 1.833; CIs [1.826, 1.842] around Julian day 11, 2015.

The delay times show an inverse trend to V_P/V_S and less variation overall (Figure 6). Prior to SSE2, the delay time increases from 0.143s; CIs [0.131s, 0.154s] to 0.178s; CIs [0.206s, 0.158s], over ~50 days. During the main SSE slip pulse, the delay time decreases from 0.178s to 0.139s; CIs [0.128s, 0.150s]. The delay time then returns to the initial value of ~0.156 over ~50 days. Similarities in the moving medians of V_P/V_S and delay time observations suggest that variations associated with the occurrence of SSEs are a regional process that can be widely observed.

To test the effects on V_P/V_S and delay time by stacking stations located on the outskirts of SSE2, we compare our results from stacking all the stations to only the stations (LOBS7, LOBS8, EOBS2, EOBS5) located in the center of the SSE and stations (LOBS3, LOBS9, EOBS1, EOBS3, EOBS4) located outside of the SSE (Figure S5). We observe a similar trend in the different station distributions, although the trend for the stack of stations located closest to the center of the SSE shows a stronger signal in both V_P/V_S and delay time, suggesting that the area of highest slip has the greatest effect on our observed measurements.

The second largest change in V_P/V_S is observed starting on day 26 (2015; Figure 6), with values increasing from 1.833; CIs [1.826, 1.842] to 1.892; CIs [1.879, 1.906] and has no matching signal in the delay time measurements. To investigate the isolated V_P/V_S change we examined earthquakes during this time and found a cluster of 31 onshore earthquakes between Julian days 36-39, 2015 (Figure S6). Earthquakes located in the same area as this cluster but at different times produce high V_P/V_S values, close to 1.9. The 20-day length of the moving window, plotted at the center of the window, causes a 10-day shift in the start of the associated V_P/V_S increase. To test for the influence of the cluster on V_P/V_S, we removed it and the resulting V_P/V_S no longer shows an increase (Figure S6). The lack of change of delay time with V_P/V_S indicates that the inverse variation in the delay time signal is essential to distinguishing physical changes from spurious variations in the data.

To test for temporal variations due to variations in earthquake locations we examine sub-catalogs of 159 earthquakes that have near-identical locations at different times (Section S4; Figure S7). Figure S8 shows the stack of earthquakes using our spatial sub-catalogs from Figure S7 for offshore (E-F) and onshore (G-H) stations. We observe similar temporal variations in V_P/V_S and δt from earthquakes occurring in our spatial sub-catalogs compared to using earthquakes from the entire catalog for offshore stations, although the confidence intervals of the former are larger (Figure S8). This result suggests that spatial variations in earthquake locations are not a major contributor to the observed V_P/V_S and δt temporal variations.

In laboratory studies, apparent V_P/V_S ratios vary considerably by changing the raypath angle, between perpendicular and parallel, relative to the crack fabric (*Wang et al.*, 2012). However, we do not observe significant changes in V_P/V_S related to varying incidence angle (Figure S9) and thus do not consider incidence angle as a contributor to the observed temporal changes.

Table 1. Average Φ, V_P/V_S, and Delay Time for Individual Stations

Station	N	$\mu(\phi)$	95% CIs	Rayleigh Test p-Value	Median V_P/V_S	95% CIs	Median δt	95% CIs
LOBS3	490	59.7°	[49.6°, 69.1°]	1.839e-8	1.835	[1.829, 1.843]	0.135s	[0.128s, 0.150s]
LOBS7	1072	19.3°	[12.8°, 26.1°]	9.262e-17	1.876	[1.869, 1.885]	0.135s	[0.124s, 0.143s]
LOBS8	1083	-7.6°	[169.0°, 175.8°]	1.077e-51	1.897	[1.885, 1.913]	0.143s	[0.139s, 0.150s]
LOBS9	851	-64.6°	[110.6°, 120.1°]	1.340e-28	1.891	[1.884, 1.906]	0.161s	[0.154s, 0.170s]
EOBS1	695	-64.9°	[99.1°, 131.1°]	1.068e-3	1.837	[1.829, 1.844]	0.210s	[0.195s, 0.240s]
EOBS2	1144	-75.1°	[-91.5°, -58.9°]	1.245e-3	1.842	[1.836, 1.847]	0.161s	[0.154s, 0.169s]
EOBS3	1146	-61.8°	[114.0°, 122.6°]	2.993e-36	1.861	[1.855, 1.868]	0.148s	[0.139s, 0.154s]
EOBS4	889	8.2°	[-3.2°, 20.2°]	5.402e-6	1.834	[1.830, 1.839]	0.165s	[0.154s, 0.169s]
EOBS5	963	-36.7°	[137.6°, 149.2°]	1.305e-19	1.899	[1.891, 1.907]	0.158s	[0.150s, 0.165s]
CNGZ	76	80.0°	[17.8°, 150.2°]	0.714	1.920	[1.882, 1.947]	0.178s	[0.150s, 0.238s]
KNZ	169	65.8°	[59.1°, 72.7°]	2.240e-13	1.876	[1.857, 1.895]	0.180s	[0.155s, 0.199s]
MHGZ	61	69.9°	[-161.5°, -11.1°]	0.664	1.873	[1.850, 1.900]	0.240s	[0.195s, 0.270s]
MWZ	385	54.6°	[43.8°, 66.5°]	9.374e-6	1.810	[1.803, 1.818]	0.124s	[0.116s, 0.135s]
PRGZ	191	11.2°	[3.6°, 18.8°]	1.623e-10	1.892	[1.869, 1.924]	0.255s	[0.219s, 0.285s]
PUZ	309	1.5°	[-4.2°, 7.1°]	1.664e-18	1.817	[1.799, 1.836]	0.176s	[0.158s, 0.200s]
RIGZ	427	-6.3°	[-15.2°, 2.3°]	9.541e-9	1.891	[1.874, 1.906]	0.194s	[0.176s, 0.205s]
TKGZ	437	83.0°	[76.5°, 90.0°]	1.439e-15	1.875	[1.855, 1.891]	0.146s	[0.135s, 0.154s]
TWGZ	288	59.1°	[46.6°, 71.3°]	2.213e-5	1.851	[1.829, 1.870]	0.180s	[0.165s, 0.195s]

Note: N: Number of A and B grade measurements and $\mu(\phi)$: circular mean of the fast azimuth (relative to North). 95% CIs: 95% confidence intervals given as [lower limit, upper limit].

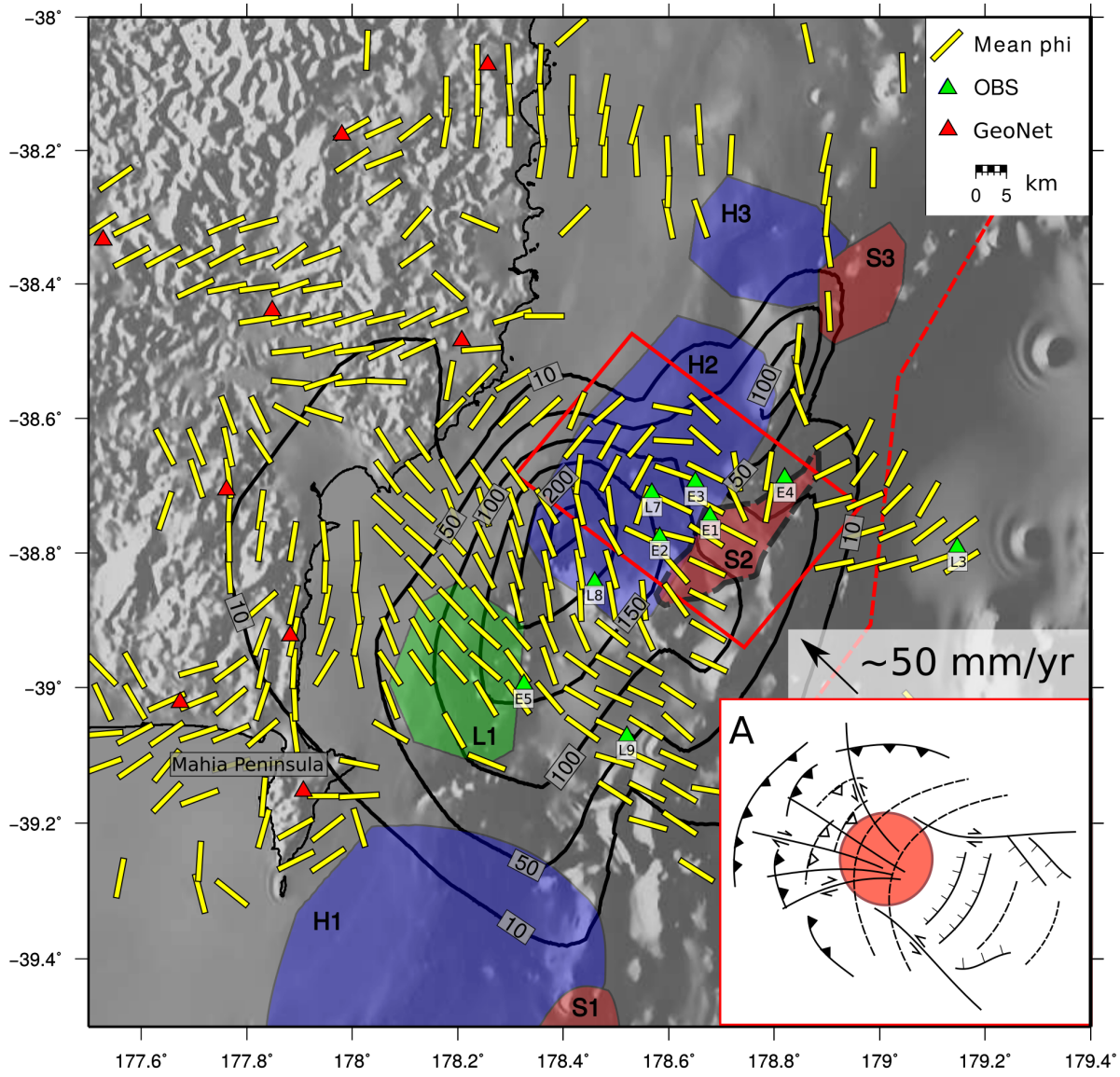

Figure 4. Spatial averages of SWS fast azimuths from TESSA (*Johnson et al.*, 2011) using the 1,893 earthquakes that are within the boundaries shown here. Yellow bars show average fast azimuths for each block plotted in the center of the grid block. Fast azimuths are not plotted for blocks with average values that have a standard deviation greater than 30° and standard error larger than 10°. Colored polygons represent features from *Bell et al.* (2010) and updated S2 from *Barker et al.* (2018); seamounts (S-red), high-amplitude reflectivity zones (H-blue) and low-amplitude reflectivity zone (L-green). Black contours show total slip during SSE2 (*Wallace et al.*, 2016). Triangles are locations of offshore and onshore seismic stations. Red dashed line marks the Hikurangi Trench (*Litchfield et al.*, 2014). Inset A shows sketch of the top view of a fracture network created by a subducting seamount, red circle, based on *Dominguez et al.* (1998). The red box highlights the area where fast azimuths resemble fracture patterns created by subducting seamounts. The black arrow shows the convergence rate between the Pacific and Central Hikurangi blocks [from *Wallace et al.* (2004)].

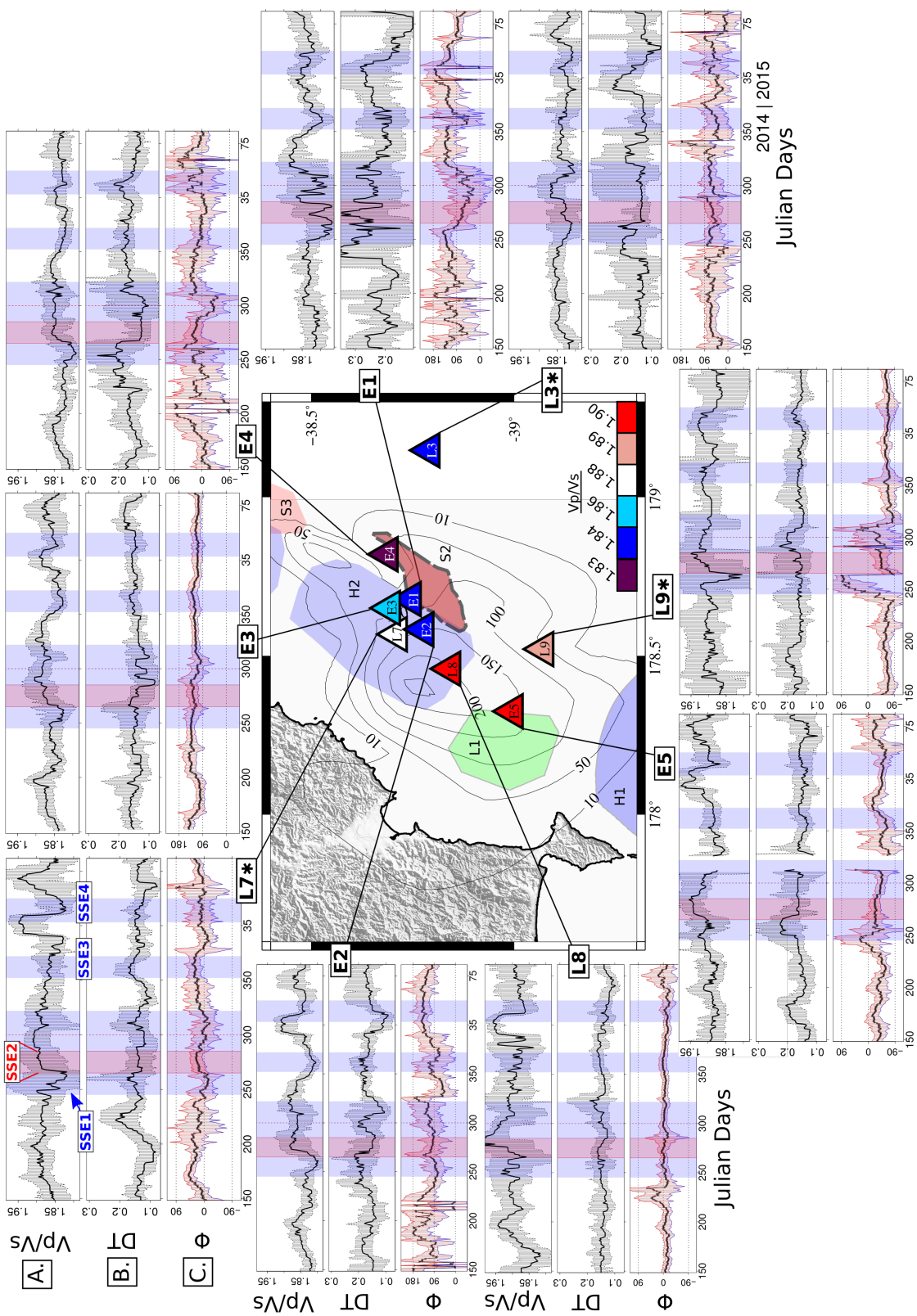

Figure 5. V_P/V_S and SWS results at HOBITSS stations. On map- *S2* and *S3* are areas of seamounts, *H1* and *H2* are high-amplitude reflectivity zones and *L1* is a lens reflectivity zone, mapped by *Bell et al.* (2010) and *Barker et al.* (2018). Triangles indicate LOBS and EOBS stations and are colored by the average V_P/V_S. Stations marked with an asterisk had timing issues, although SWS results will not be impacted (refer to Figure S1). (A) V_P/V_S. Black line is a median of 20-day moving windows with 95% confidence intervals. The main pulse of the SSE2 is shaded in red and the red dashed vertical line marks the extended duration of the low-level slip associated with this SSE. Blue rectangles indicate times of other SSEs close to our study area. (B) Delay time. Black line is a median of 20-day moving windows with 95% confidence intervals. (C) Fast azimuths. Black line is a mean of 20-day moving windows with 95% confidence intervals.

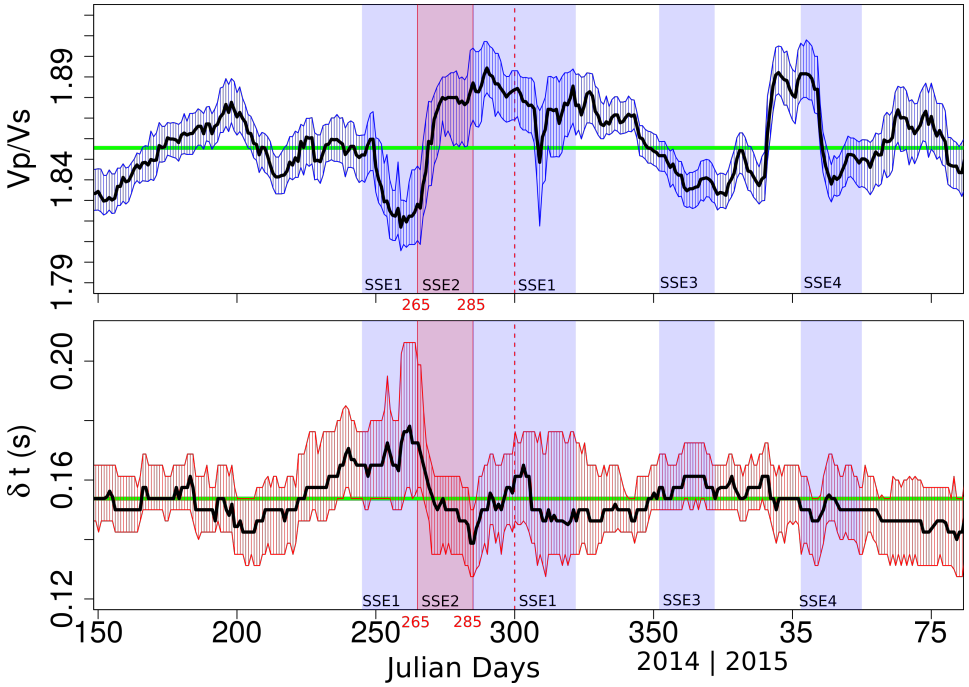

Figure 6. Top: V_P/V_S change on stack of all offshore stations for entire catalog (9,056 measurements). Blue lines indicate upper and lower 95% confidence intervals. Horizontal green line shows median V_P/V_S for all measurements. SSEs are shaded and labeled 1-4. The main pulse of SSE2 is shaded red. The red dashed vertical line marks the extended duration of the low-level slip associated with SSE2. Bottom: Delay time change on stacked offshore stations (8,333 measurements). Red lines indicate upper and lower 95% confidence intervals. Green line shows median delay time for all measurements.

5 Discussion

Most stations have a significant mean fast azimuth (Figure 3; Table 1). Mean fast azimuths from previous results by *Unglert* (2011), at onshore stations PUZ, KNZ, and MWZ (Figure 1), closely match the mean fast azimuths obtained in this study for the same stations (Figure 3). Onshore stations tend to exhibit N-S or NE-SW azimuths and are oriented parallel or sub-parallel to nearby normal faults (Figure 3; *Litchfield et al.*, 2014).

Spatial averaging (Figure 4) helps to reveal trench perpendicular fast azimuths, NW-SE, in the southeastern portion of the array, east of Mahia peninsula, into the slip region, and across stations EOBS5 (323°; CIs [317°, 329°]) and LOBS9 (296°; CIs [291°, 301°]) and the lens reflectivity zone (*Bell et al.*, 2010), *L1* (Figure 3). The NW-SE fast azimuths are sub-parallel to the convergence direction near the trench, ~294° (Pacific and Central Hikurangi blocks, *Wallace et al.*, 2004), suggesting that regional stresses, induced by plate convergence, are dominant in this region.

The fast azimuths around the seamount *S2* resemble fracture and fault patterns previously identified around subducting seamounts in both field and laboratory studies (Figure 4; Inset A; *Dominguez et al.*, 1998). Seamount *S2* spans an area of ~30 km, and the observed variable fast azimuths extend around the downdip edge of the seamount, where stresses are expected to be highest (*Baba et al.*, 2001).

The location of the high-amplitude reflectivity zone, *H2*, is consistent with shear zone deformation in front of subducting seamounts (*Baba et al.*, 2001; *Bell et al.*, 2010). The resemblance of the fast azimuths to seamount fracture patterns indicates that these directions may be structurally controlled through faulting. The complex fracture pattern and stress distribution created by subducted seamounts creates numerous connected fluid pathways that could promote slow slip around the seamount (*Shaddox and Schwartz*, 2019). *Todd et al.* (2018) found that tremor during SSE2 is localized in the vicinity of seamount *S2* and *S3* and suggest that tremor may be triggered by stress changes induced by slow slip (*Barker et al.*, 2018). There are several smaller subducted seamounts off the coast of Gisborne located in our study area (*Bell et al.*, 2010), although the raypath coverage across these seamounts is limited. Seamount *S2* is the largest in the SSE rupture area and the HOBITSS array.

Although most stations have significant mean fast azimuths, temporal variations in these azimuths are observed on stations EOBS1, 4 and LOBS9 (Figure 5). Stations EOBS1 and EOBS4 exhibit a gradual anti-clockwise rotation in Φ during SSE2, starting at ~160° at Julian day 260, decreasing to ~40° by day 290 and completing a full 180° circuit by returning to ~160° on day 300 (Figure 5). Stations EOBS1 and 4 are in close proximity to the intersection point between seamount *S2* and high-amplitude reflectivity zone *H2* and we suggest that their temporal changes are related to SSE2 and the position of these sites relative to the seamount.

The southernmost offshore station, LOBS9, is located on a bend within the slip contours and shows a clear change in Φ starting at Julian day 245, 20 days before SSE2 (Figure 5). Calculations for the Coulomb failure stress change on the plate interface show a large change in stress on the bend in the slip contours near station LOBS9 (*Todd et al.*, 2018). This change in the fast azimuth at LOBS9 might be a precursory signal, however, the change also coincides with the onset of SSE1, just south of our study area and before SSE2 (*Warren-Smith et al.*, 2019). We cannot distinguish between a precursory signal or a stress change associated with SSE1, to the south. Additionally, the 20-day moving windows used to plot the V_P/V_S, delay time, and Φ are plotted at the center of the window, so any observed changes could have started 10 days earlier or later. Although the 20-day moving windows obscure the timing of changes by ±10 days, inspection of 1-day moving windows indicates that the change in parameters does begin on day 245, 20 days before SSE2.

Crustal stress changes can occur on both a local scale, induced by earthquakes, and regional scale, caused by tectonic loading. If local and regional stresses are on the same order as, or stronger than that of structural influences, and S_Hmax is not parallel to the strike of the structure, it is possible to observe changes in S_Hmax by monitoring temporal changes in Φ as it is sensitive to the shape, orientation, and density of microcracks. Changing fast azimuths on stations EOBS1, 4 and LOBS9 are interpreted as localized rotations in microcracks due to the stress changes associated with SSEs. The lack of changes in Φ at stations that are in close proximity to stations that do exhibit a rotation suggest that stress changes

in the crust may be highly localized and channelled by existing fault structures. Local and regional changes in stress or fluid content can also cause fluctuations in delay times and V_P/V_S.

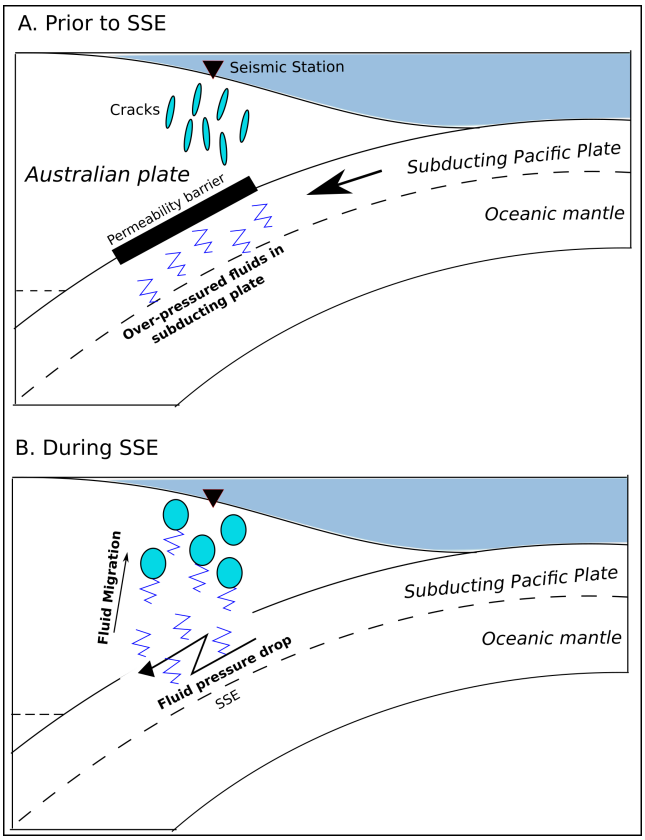

Figure 7. Model adapted after *Husen and Kissling* (2001) explaining fluid flow after the September-October 2014 SSE. Black arrow shows direction of stress along the seismogenic zone. A. Before the SSE rupture, increased stress due to convergence between plates. Near-lithostatic pore pressure pressures exist below the permeability boundary. B. After the SSE, permeability seal ruptures and fluids migrate upwards.

Our V_P/V_S value of 1.73 for the catalog, derived from the slope of the Wadati plot (i.e., $T_S - T_P$ vs T_P for all the combined data), is similar to the V_P/V_S of 1.76 reported by *Yarce et al.* (2019) and the values from the 3D velocity of *Eberhart-Phillips et al.* (2010) which range from 1.75 to 1.80 in our study area. However, our Wadati plot has a T_P intercept of ~1 second (at $T_P = 0$, $T_S/T_P = 1.0s$). The ~1 second offset indicates that earthquakes travel through material with different values of Poisson's ratio (*Kisslinger and Engdahl*, 1973). This is likely caused by slow shear velocity sediments beneath the seafloor as recently modelled by *Kaneko et al.* (2019) to explain observations of ultra-long duration ground motion observed offshore Gisborne during the 2016 Kaikoura earthquake. The material properties and intercept offset impact event-station V_P/V_S measurements as the calculation of individual T_S/T_P values assumes an intercept at the origin. We therefore obtain increased V_P/V_S from individual measurements, with the median (1.857) larger than the overall catalog V_P/V_S (1.73), from the slope of the Wadati plot.

Most offshore stations exhibit a decreasing delay time and increasing V_P/V_S during SSE2 (Figure 5). Because the majority of raypaths travel through the SSE patch, we stack the temporal delay times and V_P/V_S measurements to help reinforce variations seen at individual stations (Figure 6). Prior to SSE2, the delay time increases from 0.143s to 0.178s, over ~50 days, while the V_P/V_S decreases from 1.860 to 1.817, over ~15 days leading up to SSE2. The delay time and V_P/V_S change before SSE2 suggests there may be a recognizable precursory signal to SSEs. However, SSE1, occurring just south of our study area coincides with the change in V_P/V_S and delay time and could potentially influence these measurements. We interpret this trend in δt and V_P/V_S as changes in differential horizontal stress that act to change crack aspect ratios and orientations. Differential horizontal stress will preferentially close the cracks that are oriented orthogonal to the maximum horizontal compressive stress ($S_H max$; *Nur*, 1971). With increasing differential horizontal stresses, cracks are compressed and become vertically aligned (*Crampin*, 1981). A ray traveling through vertically aligned cracks will result in maximum anisotropy and increased delay times (*Nur*, 1971). This is consistent with our observation of increasing δt and decreasing V_P/V_S values before the initiation of SSE2. *Gao and Crampin* (2006) previously observed increasing delay times before large earthquakes and also suggest stress accumulation as a source of the increase. However, they report that following that increase, some stations exhibit a decrease in delay time, before the earthquakes, suggesting crack coalescence as an interpretation of this phenomenon. We do not observe a decreasing delay time before SSE2 and suggest stress accumulation as the main contributor to our increasing delay times before the SSE. Crack coalescence may explain the decreasing delay time during SSE2.

During SSE2, we observe a decrease in delay time, from 0.178s to 0.139s (Figure 6). The delay time then returns to a value of ~0.156s over ~50 days. While delay time decreases during SSE2, V_P/V_S increases, from 1.817 to 1.894, followed by a decrease after the SSE back to 1.833, around Julian day 11, 2015. Previous studies showing similar V_P/V_S changes have suggested that the rupture of a low-permeability seal along the plate interface driven by large earthquakes (*Husen and Kissling*, 2001) or SSEs (*Nakajima and Uchida*, 2018) could explain the variations. *Lucente et al.* (2010) reported changes in V_P/V_S linked to fluid flow across a faulted barrier, and also observed an inverse variation between V_P/V_S and delay times. A thermomechanical fluid model along 05CM-04 line in Figure 1 predicts that significant over-pressures may develop in the subduction interface if a low-permeability (10^{-20} m^2) seal is present (*Ellis et al.*, 2015). Recent work by *Warren-Smith et al.* (2019) using the HOBITSS dataset suggests that observed fluctuations in retrieved stress ratios inferred from earthquakes may indicate changes in pore fluid pressure within the subducting crust (below a possible low-permeability seal) that is related to, or perhaps controls, SSE timing. *Shaddox and Schwartz* (2019) observe repeating earthquakes occurring during SSE2, on multiple upper-plate faults within the fracture network of subducted seamount *S2*. They suggest that these earthquakes were triggered by the migration of fluid during the SSE from over-pressured sediments downdip of the seamount into the upper-plate.

Similar to *Warren-Smith et al.* (2019), we suggest that when SSE2 initiated, a low permeability seal was ruptured, allowing for fluid migration and the interconnection of fluids (i.e., crack coalescence) that were previously isolated (Figure 7). After the rupture of the permeability barrier, the pressure gradient between possible near-lithostatic pore pressure in the subducting plate/plate interface and relatively lower pore pressure in the overriding plate induces fluid transfer. The increase in V_P/V_S and decrease in delay time during SSE2 suggests that an interconnection of cracks allows for fluid transfer upwards from below the previously sealed, possibly over-pressured subducting plate. This is consistent with previous analysis of cyclic stress tensors and inferred fluid pressure changes observed from focal mechanisms analysis (*Warren-Smith et al.*, 2019), which suggests a drop in fluid pressure occurring within the subducting crust during multiple SSEs recorded during HOBITSS. With horizontal differential stresses decreasing after the onset of SSE2 and with fluids migrating upwards, cracks become rounder and more randomly oriented, consistent with a decreasing delay time and increasing V_P/V_S. After SSE2, we interpret that the drop in V_P/V_S is due to drainage of fluids from the previously fluid-rich zone.

A similar trend to our delay time and V_P/V_S was observed during the 2009 L'Aquila earthquake sequence in Italy. *Lucente et al.* (2010) observed a sudden change in V_P/V_S on several stations after the largest-magnitude foreshock. They infer that the seal between the footwall and hanging wall was broken after the foreshock, promoting fluid migration across the fault zone and filling the fractures and cracks in the hanging wall. A station located above the hanging wall of the fault exhibits a V_P/V_S rising from ~1.8 to 1.85 and decreasing back to 1.83 and a normalized delay time increasing ~15 days before the ML 4 foreshock and sharply decreasing after the foreshock.

As discussed in the introduction, *Husen and Kissling* (2001) interpret the increase in V_P/V_S ratios (over 50 days) following the main shock of the Mw 8.0 earthquake in Antofagasta, Chile as evidence of post-seismic fluid flow after the rupture of a permeability seal during the main shock of the earthquake, with near-lithostatic fluid pressures below the sealed boundary (prior to the seal breaching earthquake) causing fluids to migrate above the rupture zone, into the upper-plate. *Nakajima and Uchida* (2018) observe variations in seismic attenuation and seismicity rates with the cyclic occurrence of SSEs in Kanto, Japan. They proposed that a low-permeability seal surrounding the megathrust fails during SSEs and drainage saturates the rock above, resulting in increased supraslab seismicity and attenuation in the area (*Nakajima and Uchida*, 2018). The break is then resealed by cementation and pore-fluid pressures in the megathrust begin to increase, eventually leading to the next phase of failure. Our V_P/V_S and delay time changes support suggestions by *Warren-Smith et al.* (2019) that a similar process may be at work in Hikurangi.

Husen and Kissling (2001) report an estimated permeability value of 10^{-16}-10^{-17} m^2, given a time period of 50 days between the main shock and the appearance of the high V_P/V_S ratios and a fluid migration distance of 20 km. *Nakajima and Uchida* (2018) estimate a permeability of 2-4 x 10^{-14} m^2 for a time range of 0.2-0.4 years and a fluid migration distance of 5 km, 2-3 orders of magnitude larger com-

pared to that estimated by *Husen and Kissling* (2001). To estimate the permeability in the September-October 2014 SSE (SSE2) region, we use the relation from *Townend and Zoback* (2000) and modified by *Nakajima and Uchida* (2018), $k = \beta\eta l^2/\tau$. Permeability (k) is expressed as a function of time (τ), fluid migration distance (l), specific storage coefficient (β), and dynamic viscosity (η). Given a time of 20 days, in which the V_P/V_S increased during SSE2, a fluid migration distance between 0.5-4 km, based on the range of depths where the majority of the repeating earthquakes occurred (e.g., 3-7 km depth; *Shaddox and Schwartz*, 2019), (β) of 10^{-10} Pa^{-1} for low porosity rock, and dynamic viscosity (η) of 10^{-4} Pa s, we obtain a permeability between 0.1 x 10^{-14} and 9 x 10^{-14} m^2. Such high permeability values suggest a highly fractured network of cracks in the overriding plate. Despite the slow rupture velocity, we propose that the September-October 2014 SSE was capable of rupturing enough of the permeability seal to induce fluid flow, consistent with our observed increase in V_P/V_S.

6 Conclusions

We calculated SWS and V_P/V_S ratios for event-station pairs using local earthquakes recorded, for the first time, on OBSs located above a shallow, 5-week long, offshore SSE on the Hikurangi subduction zone. Our findings suggest that spatial variations in fast azimuths are affected by stress and structures in the region and that stress changes and fluid migration during SSEs are detectable with SWS and V_P/V_S analyses.

Spatial averaging shows regional stress directions in much of the offshore area, parallel to the relative plate convergence directions, but with a variation around subducted seamount, *S2*. This variation is consistent with fault and fracture patterns created by subducting seamounts observed in laboratory and field experiments. The resemblance of the fast azimuths to seamount fracture patterns suggests some structural control through faulting. The upper-plate fracture network above the subducted seamount is the host of migrating fluids, from over-pressured sediments downdip of the seamount, resulting in a complicated environment of stress distribution (*Shaddox and Schwartz*, 2019).

Temporal changes in fast azimuths at individual stations are observed around the time of the main SSE. Of these stations, EOBS1 and 4, located on the border between seamount, *S2*, and a high-amplitude reflectivity zone, *H2*, show a change occurring during the September-October 2014 SSE (SSE2). We interpret the changes in Φ at these stations as a rotation in microcracks corresponding to stress changes associated with SSEs. The temporal variations in Φ at individual stations, along with the similarity of spatial averaging fast azimuths to structural patterns around the subducting seamount, suggest a combination of stress and structural effects due to the interactions of subducting seamounts with the overriding plate. The lack of observed changes at other nearby stations indicate that areas of stress change can be highly localized and complex.

Temporal variations in V_P/V_S and delay time measurements are observed on individual OBS stations during the September-October 2014 SSE. Stacking measurements across all offshore stations en-

hanced our signal and revealed clear opposing trends in delay time and V_P/V_S. The stacked signal also indicates that the changes may occur over a broad region. Similar to *Warren-Smith et al.* (2019), we suggest that during the SSE a low permeability seal on the plate interface is ruptured, allowing for the interconnection of fluids. *Shaddox and Schwartz* (2019) propose that repeating earthquakes observed above seamount *S2* were triggered by fluid migration from over-pressured sediments downdip of the seamount into the upper-plate during the SSE. The increase in V_P/V_S and decrease in delay time during the SSE suggests fluid transfer from the subducting plate, below the sealed fault zone. These observations are consistent with fluctuations in retrieved stress ratios, which indicate changes in pore fluid pressure in the subducting crust, during multiple SSEs recorded by the HOBITSS experiment (*Warren-Smith et al.*, 2019). Following the end of SSE2, a decreasing V_P/V_S may indicate the drainage of fluids from the over-pressurized fluid-rich crust. Our observations support the suggestion that the September-October 2014 SSE may have ruptured a permeability seal, and induced fluid flow.

Our findings show that temporal changes in V_P/V_S, delay time, and fast azimuths are detectable during SSEs and provide further evidence that fluids and stresses play a significant role in SSE nucleation and propagation. The inverse variation of V_P/V_S and delay time measurements allows distinction between physical variations and variations in data. We recommend that future SSE monitoring studies should consider similar network configurations to study events of similar size. Larger regional networks could help define the spatial extent of observed changes. These results also demonstrate that SWS and V_P/V_S are effective tools for investigating stress changes associated with slow slip.

Acknowledgments

We acknowledge support from an MBIE Endeavour Fund grant (funding contract C05X1605). Additional funding support came from National Science Foundation (NSF) grants: NSF-1551683, OCE-1333025, OCE-1334654, and OCE-1551922. K.M. was funded by ERI JURP 2013-B-09. The ocean bottom seismic data was provided by instruments from the Ocean Bottom Seismograph Instrument Pool (www.obsip.org) funded by the National Science Foundation (NSF), the Earthquake Research Institute (ERI), University of Tokyo, and New Zealand's GeoNet project. Raw data from the experiment is archived at Incorporate Research Institutions for Seismology Data Management Center (IRIS-DMC) with experiment codes YH 2014-15 (seismic data) and 8F 2014-15 (bottom pressure record data).

We would like to acknowledge the earthquake database used in this study and put together by Jefferson Yarce. The database is publicly available and can be found at

https://zenodo.org/record/2022405#.XIbszRNKgWo. A table of our shear wave splitting and V_P/V_S results can be found at `https://zenodo.org/record/3383417\#.XWyko3Uzbys`. We thank ERI for providing Hubert Zal and Martha Savage with fellowships as visiting researchers and stimulating valuable discussion that significantly improved the manuscript. We would also like to thank Emily-Warren Smith and Carolyn Boulton for their helpful feedback and discussion.

References

Altman, D., T. David, and M. Bryant (2000), Gardner. Statistics with confidence.

Audet, P., M. G. Bostock, D. C. Boyarko, M. R. Brudzinski, and R. M. Allen (2010), Slab morphology in the Cascadia fore arc and its relation to episodic tremor and slip, *Journal of Geophysical Research: Solid Earth*, *115*(B4), doi:10.1029/2008JB006053, b00A16.

Audoine, E., M. K. Savage, and K. Gledhill (2004), Anisotropic structure under a back arc spreading region, the Taupo Volcanic Zone, New Zealand, *Journal of Geophysical Research: Solid Earth*, *109*(B11), doi:10.1029/2003JB002932, b11305.

Baba, T., T. Hori, S. Hirano, P. R. Cummins, J.-O. Park, M. Kameyama, and Y. Kaneda (2001), Deformation of a seamount subducting beneath an accretionary prism: Constraints from numerical simulation, *Geophysical Research Letters*, *28*(9), 1827–1830, doi:10.1029/2000GL012266.

Babuska, V., and M. Cara (1991), *Seismic anisotropy in the Earth*, vol. 10, Springer Science & Business Media, doi:10.1007/978-94-011-3600-6.

Barker, D. H. N., R. Sutherland, S. Henrys, and S. Bannister (2009), Geometry of the Hikurangi subduction thrust and upper plate, North Island, New Zealand, *Geochemistry, Geophysics, Geosystems*, *10*(2), doi:10.1029/2008GC002153.

Barker, D. H. N., S. Henrys, F. Caratori Tontini, P. M. Barnes, D. Bassett, E. Todd, and L. Wallace (2018), Geophysical Constraints on the Relationship Between Seamount Subduction, Slow Slip, and Tremor at the North Hikurangi Subduction Zone, New Zealand, *Geophysical Research Letters*, *45*(23), 12,804–12,813, doi:10.1029/2018GL080259.

Bassett, D., R. Sutherland, and S. Henrys (2014), Slow wavespeeds and fluid overpressure in a region of shallow geodetic locking and slow slip, Hikurangi subduction margin, New Zealand, *Earth and Planetary Science Letters*, *389*, 1 – 13, doi:10.1016/j.epsl.2013.12.021.

Beanland, S., and J. Haines (1998), The kinematics of active deformation in the North Island, New Zealand, determined from geological strain rates, *New Zealand Journal of Geology and Geophysics*, *41*(4), 311–323, doi:10.1080/00288306.1998.9514813.

Bell, R., R. Sutherland, D. H. N. Barker, S. Henrys, S. Bannister, L. Wallace, and J. Beavan (2010), Seismic reflection character of the Hikurangi subduction interface, New Zealand, in the region of repeated Gisborne slow slip events, *Geophysical Journal International*, *180*(1), 34–48, doi:10.1111/j.1365-246X.2009.04401.x.

Coffin, M., L. Gahagan, and L. Lawver (1998), Present-day plate boundary digital data compilation, *University of Texas Institute for geophysics technical report*, *174*(5).

Crampin, S. (1981), A review of wave motion in anisotropic and cracked elastic-media, *Wave Motion*, *3*(4), 343 – 391, doi:10.1016/0165-2125(81)90026-3.

Crotwell, H. P., T. J. Owens, and J. Ritsema (1999), The TauP Toolkit: Flexible Seismic Travel-time and Ray-path Utilities, *Seismological Research Letters*, *70*(2), 154, doi:10.1785/gssrl.70.2.154.

Dominguez, S., S. Lallemand, J. Malavieille, and R. von Huene (1998), Upper plate deformation associated with seamount subduction, *Tectonophysics*, *293*(3), 207 – 224, doi:10.1016/S0040-1951(98)00086-9.

Eberhart-Phillips, D., M. Reyners, S. Bannister, M. Chadwick, and S. Ellis (2010), Establishing a Versatile 3-D Seismic Velocity Model for New Zealand, *Seismological Research Letters*, *81*(6), 992–1000, doi:10.1785/gssrl.81.6.992.

Eberhart-Phillips, D., S. Bannister, and M. Reyners (2017), Deciphering the 3-D distribution of fluid along the shallow Hikurangi subduction zone using P-and S-wave attenuation, *Geophysical Journal International*, *211*(2), 1054–1067, doi:10.1093/gji/ggx348.

Ellis, S., A. Fagereng, D. Barker, S. Henrys, D. Saffer, L. Wallace, C. Williams, and R. Harris (2015), Fluid budgets along the northern Hikurangi subduction margin, New Zealand: the effect of a subducting seamount on fluid pressure, *Geophysical Journal International*, *202*(1), 277–297, doi:10.1093/gji/ggv127.

Gao, Y., and S. Crampin (2006), A stress-forecast earthquake (with hindsight), where migration of source earthquakes causes anomalies in shear-wave polarisations, *Tectonophysics*, *426*(3), 253 – 262, doi:10.1016/j.tecto.2006.07.013.

Head, T. J. (2001), The nature of shallow anisotropy in the southern Raukumara Peninsula, New Zealand, determined by shear-wave splitting measurements from local earthquakes, Master's thesis, University of Leeds, Leeds, UK.

Husen, S., and E. Kissling (2001), Postseismic fluid flow after the large subduction earthquake of Antofagasta, Chile, *Geology*, *29*(9), 847–850, doi:10.1130/0091-7613(2001)029<0847:PFFATL>2.0.CO;2.

Johnson, J. H., M. K. Savage, and J. Townend (2011), Distinguishing between stress-induced and structural anisotropy at Mount Ruapehu volcano, New Zealand, *Journal of Geophysical Research: Solid Earth*, *116*(B12), doi:10.1029/2011JB008308, b12303.

Kaneko, Y., Y. Ito, B. Chow, L. M. Wallace, C. Tape, R. Grapenthin, E. D'Anastasio, S. Henrys, and R. Hino (2019), Ultra-long duration of seismic ground motion arising from a thick, low velocity sedimentary wedge, *Journal of Geophysical Research: Solid Earth*, doi:10.1029/2019JB017795.

Kisslinger, C., and E. R. Engdahl (1973), The interpretation of the Wadati diagram with relaxed assumptions, *Bulletin of the Seismological Society of America*, *63*(5), 1723–1736.

Litchfield, N., R. V. Dissen, R. Sutherland, P. Barnes, S. Cox, R. Norris, R. Beavan, R. Langridge, P. Villamor, K. Berryman, M. Stirling, A. Nicol, S. Nodder, G. Lamarche, D. Barrell, J. Pettinga, T. Little, N. Pondard, J. Mountjoy, and K. Clark (2014), A model of active faulting in New Zealand, *New Zealand Journal of Geology and Geophysics*, *57*(1), 32–56, doi:10.1080/00288306.2013.854256.

Lucente, F. P., P. De Gori, L. Margheriti, D. Piccinini, M. Di Bona, C. Chiarabba, and N. Piana Agostinetti (2010), Temporal variation of seismic velocity and anisotropy before the 2009 MW 6.3 L'Aquila earthquake, Italy, *Geology*, *38*(11), 1015–1018, doi:10.1130/G31463.1.

Nakajima, J., and N. Uchida (2018), Repeated drainage from megathrusts during episodic slow slip, *Nature Geoscience*, *11*(5), 351, doi:10.1038/s41561-018-0090-z.

Nur, A. (1971), Effects of stress on velocity anisotropy in rocks with cracks, *Journal of Geophysical Research*, *76*(8), 2022–2034, doi:10.1029/JB076i008p02022.

Nuttli, O. (1961), The effect of the earth's surface on the S wave particle motion, *Bulletin of the Seismological Society of America*, *51*(2), 237–246.

Obara, K., and A. Kato (2016), Connecting slow earthquakes to huge earthquakes, *Science*, *353*(6296), 253–257, doi:10.1126/science.aaf1512.

Rumpker, G., and P. G. Silver (1998), Apparent shear-wave splitting parameters in the presence of vertically varying anisotropy, *Geophysical Journal International*, *135*(3), 790–800, doi:10.1046/j.1365-246X.1998.00660.x.

Savage, M. K., A. Wessel, N. A. Teanby, and A. W. Hurst (2010), Automatic measurement of shear wave splitting and applications to time varying anisotropy at Mount Ruapehu volcano, New Zealand, *Journal of Geophysical Research: Solid Earth*, *115*(B12), doi:10.1029/2010JB007722, b12321.

Shaddox, H. R., and S. Y. Schwartz (2019), Subducted seamount diverts shallow slow slip to the forearc of the northern Hikurangi subduction zone, New Zealand, *Geology*, *47*(5), 415–418, doi:10.1130/G45810.1.

Silver, P. G., and W. W. Chan (1991), Shear wave splitting and subcontinental mantle deformation, *Journal of Geophysical Research: Solid Earth*, *96*(B10), 16,429–16,454, doi:10.1029/91JB00899.

Stachnik, J. C., A. F. Sheehan, D. W. Zietlow, Z. Yang, J. Collins, and A. Ferris (2012), Determination of New Zealand Ocean Bottom Seismometer Orientation via Rayleigh-Wave Polarization, *Seismological Research Letters*, *83*(4), 704, doi:10.1785/0220110128.

Teanby, N. A., J.-M. Kendall, and M. van der Baan (2004), Automation of Shear-Wave Splitting Measurements using Cluster Analysis, *Bulletin of the Seismological Society of America*, *94*(2), 453, doi:10.1785/0120030123.

Todd, E. K., S. Y. Schwartz, K. Mochizuki, L. M. Wallace, A. F. Sheehan, S. C. Webb, C. A. Williams, J. Nakai, J. Yarce, B. Fry, S. Henrys, and Y. Ito (2018), Earthquakes and Tremor Linked to Seamount Subduction During Shallow Slow Slip at the Hikurangi Margin, New Zealand, *Journal of Geophysical Research: Solid Earth*, *123*(8), 6769–6783, doi:10.1029/2018JB016136.

Townend, J., and M. D. Zoback (2000), How faulting keeps the crust strong, *Geology*, *28*(5), 399–402, doi:10.1130/0091-7613(2000)28<399:HFKTCS>2.0.CO;2.

Townend, J., S. Sherburn, R. Arnold, C. Boese, and L. Woods (2012), Three-dimensional variations in present-day tectonic stress along the Australia-Pacific plate boundary in New Zealand, *Earth and Planetary Science Letters*, *353-354*, 47 – 59, doi:10.1016/j.epsl.2012.08.003.

Unglert, K. (2011), Crustal cracks in areas of active deformation: Correlation of GPS and seismic anisotropy, Master's thesis, Victoria University of Wellington, NZ.

Wadati, K., and S. Oki (1933), On the travel time of earthquake waves.(Part II), *Journal of the Meteorological Society of Japan. Ser. II*, *11*(1), 14–28, doi:10.2151/jmsj1923.11.1{_}14.

Wallace, L. M., and J. Beavan (2010), Diverse slow slip behavior at the Hikurangi subduction margin, New Zealand, *Journal of Geophysical Research: Solid Earth*, *115*(B12), doi:10.1029/2010JB007717, b12402.

Wallace, L. M., and D. Eberhart-Phillips (2013), Newly observed, deep slow slip events at the central Hikurangi margin, New Zealand: Implications for downdip variability of slow slip and tremor, and relationship to seismic structure, *Geophysical Research Letters*, *40*(20), 5393–5398, doi:10.1002/2013GL057682.

Wallace, L. M., J. Beavan, R. McCaffrey, and D. Darby (2004), Subduction zone coupling and tectonic block rotations in the North Island, New Zealand, *Journal of Geophysical Research: Solid Earth*, *109*(B12), doi:10.1029/2004JB003241.

Wallace, L. M., S. C. Webb, Y. Ito, K. Mochizuki, R. Hino, S. Henrys, S. Y. Schwartz, and A. F. Sheehan (2016), Slow slip near the trench at the Hikurangi subduction zone, New Zealand, *Science*, *352*(6286), 701–704, doi:10.1126/science.aaf2349.

Wallace, L. M., S. Hreinsdottir, S. Ellis, I. Hamling, E. D'Anastasio, and P. Denys (2018), Triggered Slow Slip and Afterslip on the Southern Hikurangi Subduction Zone Following the Kaikoura Earthquake, *Geophysical Research Letters*, *45*(10), 4710–4718, doi:10.1002/2018GL077385.

Wang, X.-Q., A. Schubnel, J. Fortin, E. C. David, Y. Guéguen, and H.-K. Ge (2012), High Vp/Vs ratio: Saturated cracks or anisotropy effects?, *Geophysical Research Letters*, *39*(11), doi:10.1029/2012GL051742.

Warren-Smith, E., B. Fry, L. Wallace, E. Chon, S. A. Henrys, A. F. Sheehan, K. Mochizuki, S. Y. Schwartz, and S. Lebedev (2019), Episodic stress and fluid pressure cycling in subducting oceanic crust during slow slip, *Journal of Geophysical Research: Solid Earth*, doi:10.1038/s41561-019-0367-x.

Williams, C. A., D. Eberhart-Phillips, S. Bannister, D. H. N. Barker, S. Henrys, M. Reyners, and R. Sutherland (2013), Revised Interface Geometry for the Hikurangi Subduction Zone, New Zealand, *Seismological Research Letters*, *84*(6), 1066, doi:10.1785/0220130035.

Yarce, J., A. F. Sheehan, J. S. Nakai, S. Y. Schwartz, K. Mochizuki, M. K. Savage, L. M. Wallace, S. A. Henrys, S. C. Webb, Y. Ito, R. E. Abercrombie, B. Fry, H. Shaddox, and E. K. Todd (2019), Seismicity at the Northern Hikurangi Margin, New Zealand, and Investigation of the Potential Spatial and Temporal Relationships With a Shallow Slow Slip Event, *Journal of Geophysical Research: Solid Earth*, *124*(5), 4751–4766, doi:10.1029/2018JB017211.

Zietlow, D. W. (2016), Four Brothers and a Waka: Investigating Lithospheric Accommodation of Shear and Convergence Underlying the South Island of New Zealand, Ph.D. thesis, University of Colorado at Boulder.